Supplementary Information

Phosphorene-like InP_3 Monolayer: Structure, Stability, and Catalytic Properties toward Hydrogen Evolution Reaction

Abdul Jalil,[a] Zhiwen Zhuo, [a] Zhongti Sun,[a] Fang Wu,[b] Chuan Wang,[c]* and Xiaojun Wu[a]*

a Hefei National Laboratory of Physical Sciences at the Microscale, School of Chemistry and Materials Sciences, CAS Key Laboratory of Materials for Energy Conversion, and CAS Excellence in Nano-sciences, University of Science and Technology of China, Hefei, Anhui 230026, P. R. China
b College of Information Science and Technology, Nanjing Forestry University, Nanjing, Jiangsu 210037, P. R. China
c Institute of Advanced Synthesis, School of Chemistry and Molecular Engieering, Jiangsu National Synergetic Innovation Center for Advanced Materials, Nanjing Tech University, Nanjing 211816, Jiangsu, P. R. China

Table S1. Lattice parameters **a** & **b** (Å) total energy per atom E (eV/atom) parallel and perpendicular bond length of In-P (Å).

Methods	**Structures**	**a**	**b**	**Energy**	**Bond length**			
					In-P∥	In-P⊥	P-P∥	P-P⊥
HSE06+optB88-vdW	P-InP_3	8.13	7.51	-3.75	2.66	2.64	2.20	2.25
	G-InP_3	7.53	7.53	-3.61	2.55	----	2.23	-----
PBE+optB88-vdW	Bulk	7.58	7.58	-3.25	2.70	----	2.23	----
	P-InP_3	8.15	7.56	-3.00	2.69	2.68	2.22	2.27
	G-InP_3	7.58	7.58	-2.83	2.60	-----	2.24	-----

Exfoliation energy calculation

It is complicated for the situations to separate a monolayer or ultra-thin sheet from the bulk or a slab. Besides the exact value of exfoliation energy changes with various situations, no mention the lack of knowledge on the exact exfoliation process on experiment microscopically, such as the interface interaction of the surface of target material and the surfaces of the exfoliating tools. Here, we consider the exfoliation energy calculation in two models: (a) the ideal exfoliation energy model[1] to obtain the ideal value and (b) the "frozen atom model" to evaluate the upper limit value.

Based on the work of J. H. Jung, *et al*[1], we can get the ideal exfoliation energy for exfoliating 2D structure from bulk structures without considering the interface interaction of the surface of target material and the surfaces of the exfoliating tools. The ideal exfoliation energy is calculated by the equation of the n-layer exfoliation energy per unit area $E_{exf}(n)$ from a bulk is given by

$$E_{exf}(n)=\frac{E_{iso}(n)-E_{bulk}n/m}{A} \quad (1)$$

where $E_{iso}(n)$ is the energy of the unit cell of an isolated n-layer slab in vacuum, E_{bulk} is the energy of the unit cell of a bulk material composed of m layers, thus $E_{bulk/m}$ corresponds to the energy of the bulk per layer, and $\boldsymbol{A}$ is the in-plane area of the bulk unit cell.

Based on this method, we have calculated the exfoliation energy with optb88 as well as DFT-D3 methods, as showed in **Figure S1(a) and (b)** and Table S1. The calculated E_{exf} of P-InP_3 is 1.08 Jm^{-2}, smaller than the value (1.37 Jm^{-2}) obtained by method we used before.

We also considered the monolayer exfoliating from slab with limited thickness, such as bilayer and trilayer. Based on equation (1), we can conclude a new equations for exfoliation energy ($E_{exf}(n//n+m)$) calculation on case of ultrathin layer (n-layer) exfoliated from limited layer slab (n+m layer):

$$E_{exf}(n//n+m)=\frac{E_{iso}(n)+E_{iso}(m)-E_{iso}(n+m)}{A(n+m)} \quad (2)$$

where $E_{iso}(n)$, $E_{iso}(m)$ and $E_{iso}(n+m)$ is the energy of the unit cell of an isolated n-layer slab, m-layer slab and (n+m)-layer slab in vacuum, respectively, and $\boldsymbol{A}(n+m)$ is the in-plane area of the unit cell of (n+m)-layer slab.

With the new equation in expansion, the $E_{exf}(1//2)$ and $E_{exf}(1//3)$ of P-InP_3 and $E_{exf}(1//2)$ and $E_{exf}(1//3)$ of G-InP_3 is shown in **Figure S1(a) and (b)** and **Table S1**.

Considered the real process with complicated situations, the upper limit value of exfoliation energy is also very important for practice to deal with all situations. Therefore a method can estimate the upper limit value for practice is used. We call this method the "frozen atom model", of which all atoms are frozen during the surfaces separating process from a bulk. Due to it has no x-y plane and surface relaxation, we can obtain an upper limit value of exfoliation energy for experimental practice. The calculated value is shown as Figure S1(c).

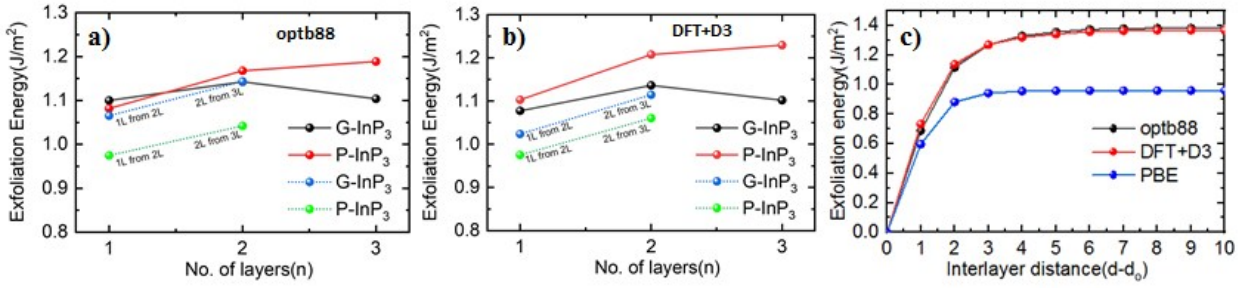

Figure S1: Exfoliation energy with ideal exfolation model with (a) optb88 (b) DFT+D3 functionals and with (c) The frozen atom model with three different functionals.

Table S2. Exfoliation energy of G- & P-InP_3 structures calculated by ideal exfoliation energy model.

Structures	**Exfoliation Energy(Jm^{-2})**	**Structures**	**Exfoliation Energy(Jm^{-2})**
G-1L	1.10	P-1L	1.08
G-2L	1.14	P-2L	1.17
G-3L	1.10	P-3L	1.19
1L from 2L	1.07	1L from 2L	0.98
1L from 3L*	1.14	1L from 3L*	1.04

* for 1L from 3L, it is equal to 2L form 3L, because they happen in same process:

3L -> 1L + 2L

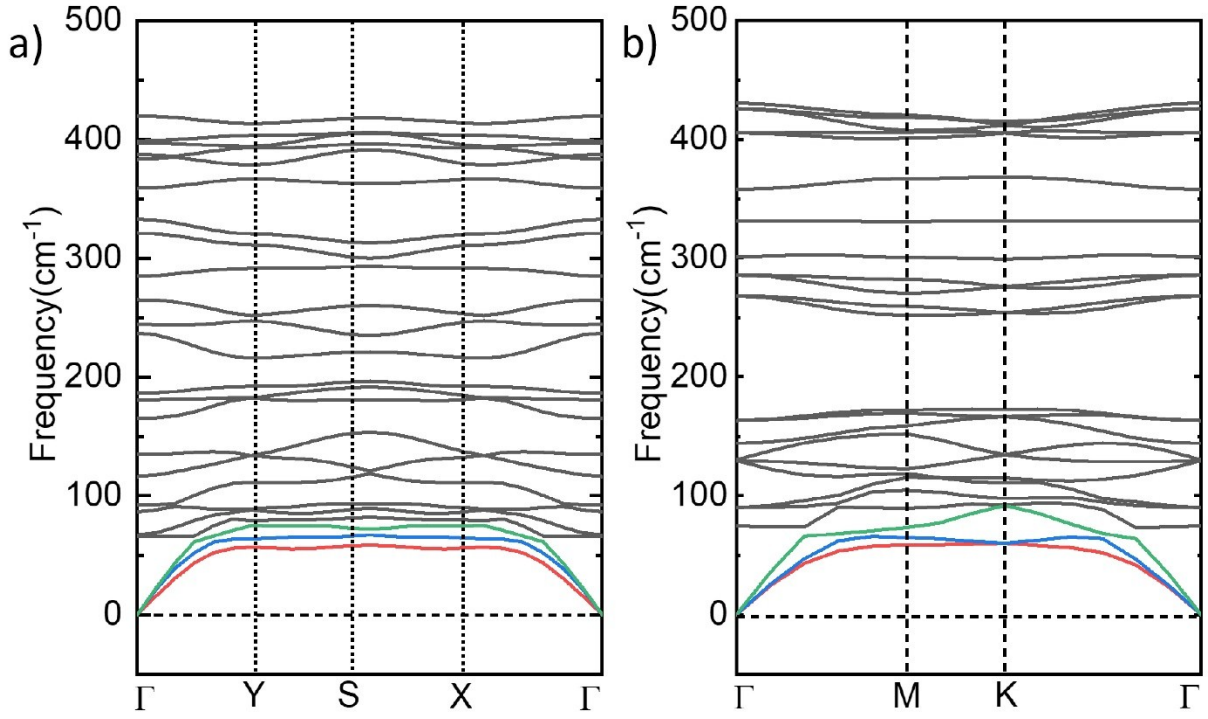

Figure S2. Lattice dynamical stability of (a) P-InP_3 and (b) G-InP_3

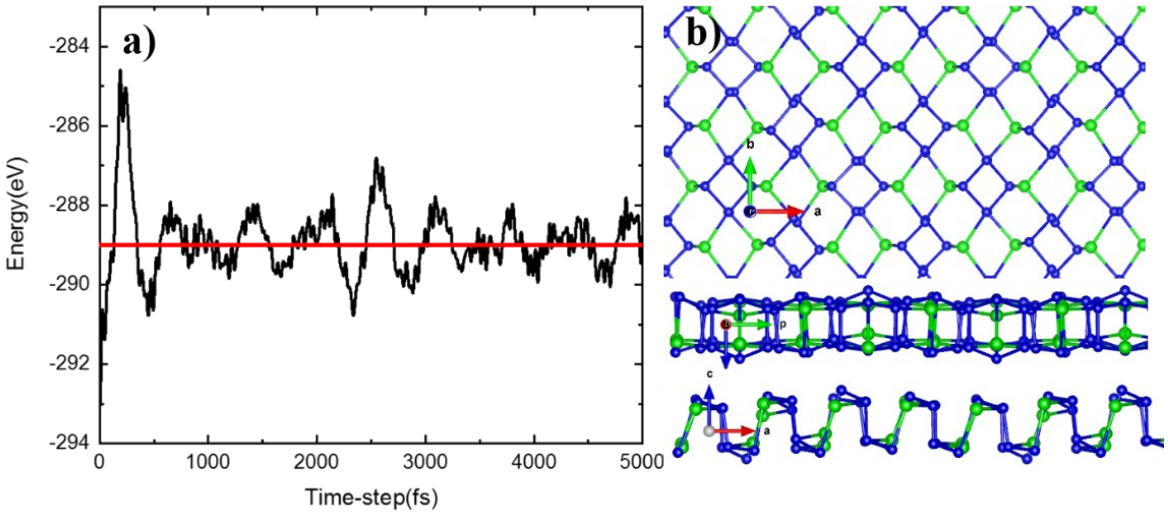

Figure S3. (a) Variation of free energy during MD simulation with total time of 5ps at 500 K. (b) Snapshots in different directions after MD simulation of structure of InP_3 monolayer at 500 K at 5ps.

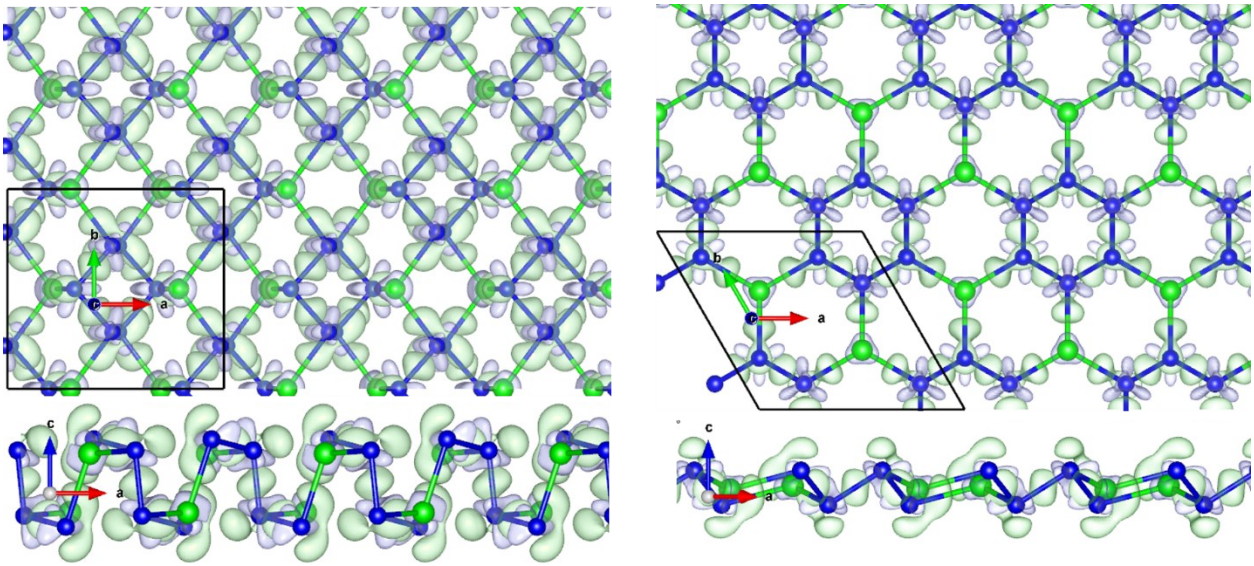

Figure S4. Deformation charge density of (a) P-InP_3 and (b) G-InP_3

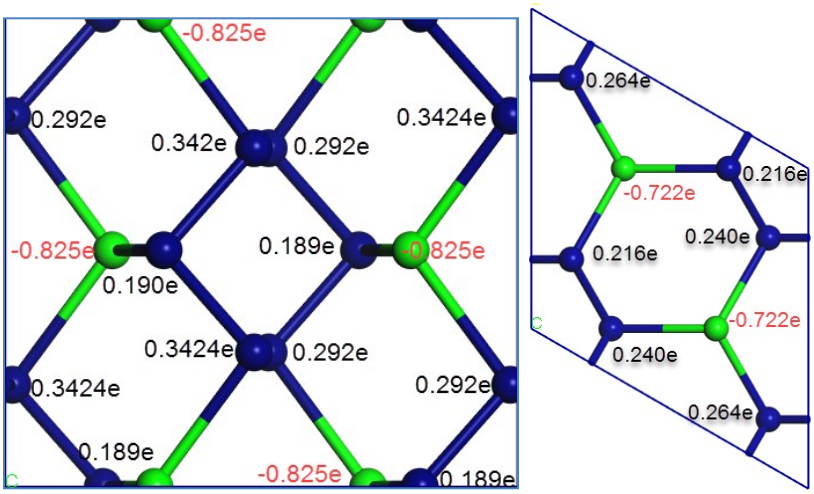

Figure S5. Charge analysis of P-InP_3 and G-InP_3 structures.

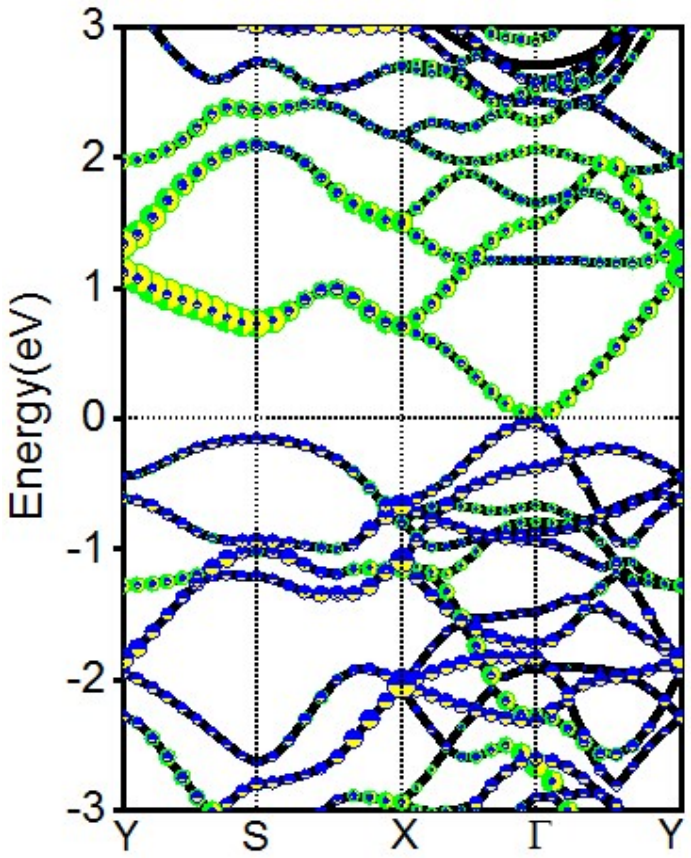

Figure S6. Electronic Band structure of P-InP_3 with PBE+optB88. (Green and blue lines indicate In and P atoms, respectively)

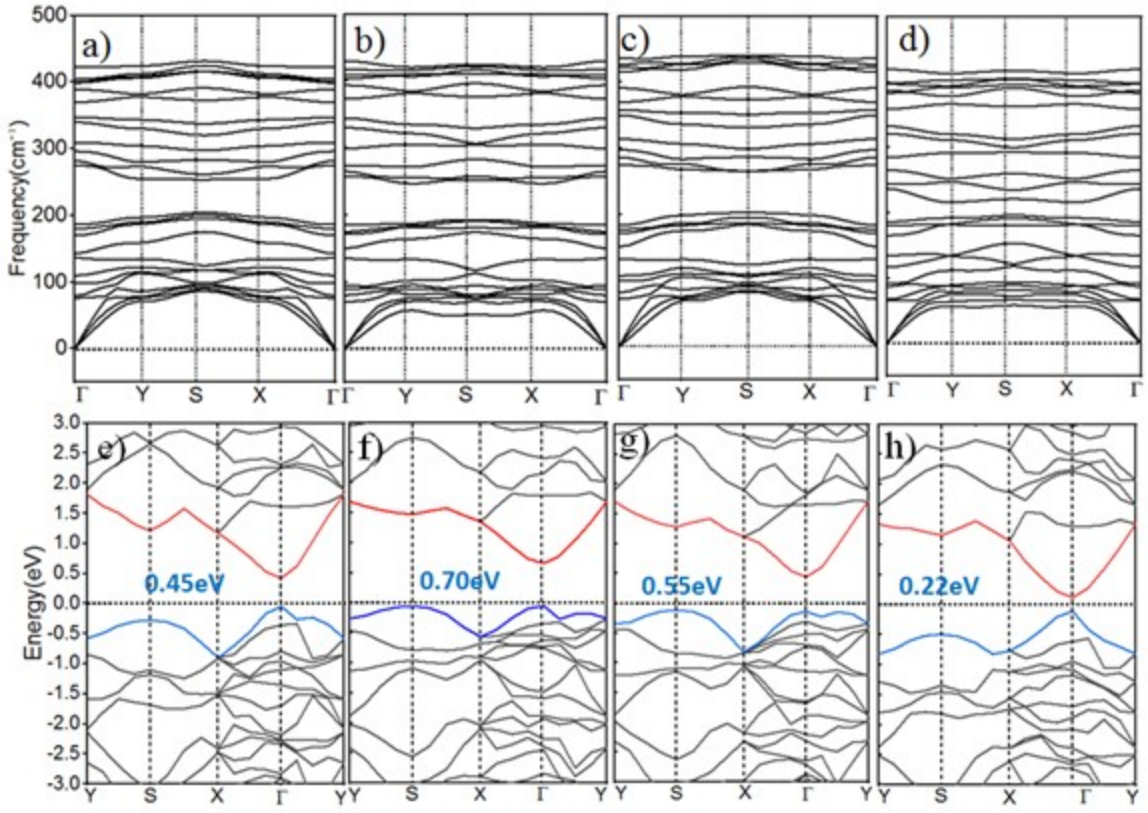

Figure S7. Lattice dynamical stability and the effect on band structure of compressive and tensile uniaxial strain (5%) on P-InP_3 structure. The phonon dispersions are result of strain at (a) -5%, (b) +5% in armchair and (c) -5%, (d) +5% in zigzag direction, respectively. The band structures are result of strain at (e) -5%, (f) +5% in armchair and (g) -5%, (h) +5% in zigzag direction, respectively.

Electron hole Mobility of P-InP_3

The mobilities of electrons and holes are directly correlated to the shift of coduction and valance band. Phonon scattering occurs when acoustic phonon wavelength dominates the bond length of crystal structure as described in Deformation potential theory[2]. The deformation potential theory has been extensively applied to

study the carrier mobility of 2D and one-dimensional (1D) materials.[3-8] For 2D systems, the analytical expressions for carrier mobility (μ) were derived as below:

$$\mu_{2D} = \frac{e\hbar^3 C_{2D}}{k_B T m^* m_d (E_l)^2} \quad (3)$$

where $\hbar$ is planks constant, T is the temperature, which is 300 K here, m* is the effective mass of charge defined as, $m^* = \hbar^2(\partial_2 E(k)/\partial k^2)^{-1}$,$\mathbf{C_{2D}}$ is stretching modulus given as $C_{2D} = (\partial^2 E_{total}/\partial \varepsilon^2)/S_0$, where S_o is the area of the lattice while a_o is the lattice constatnts in one dimension. Change in energy with strain can be calculated by quardatic fitting of total energy with respect to applied strain. The $E_1 = \partial E_{edge}/\partial \varepsilon$ is deformation potential, which can be calculated by shifting of VBM and CBM. k_B is boltzman constant.

Due to the band gap of PBE+opb88 method is too narrow to investigate the deformation potential of VBM and CBM, the HSE06+optb88 method was applied in mobility calculation. The atomic positions are relaxed during during dilation of lattice constants, and the total energies are computed by using HSE06 method with K-mesh 4×4×1. The 2D modulus (C) is attained by the quardatic fitting of total energy verses strain. The Deformation potential $\mathbf{E_1}$ for holes at VBM and for electrons at CBM are calculated by shifting of bandages due to applied strain. The elastic constants of InP_3 in armchair and zigzad directions are 40.09 Nm^{-1} and 80.69 Nm^{-1} due to the different bond strength leads the structure to anistropic features the deformational potential and elastic modulus. From **Figure-S8** the effect of strain on E_1 in both armchair and zigzag directions are different. The change of deformation potential can be analysed from charge density of CBM and VBM[5]. All results are showed as **Table S4**.

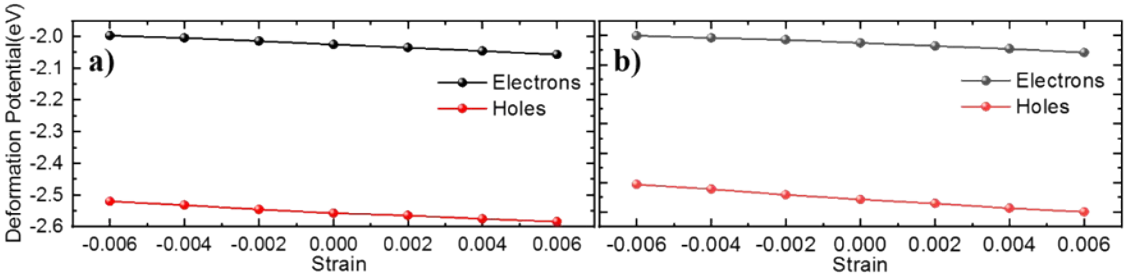

Figure S8. Shift of deformation potential to strain of P-InP_3

Table S3. E_1 (eV) deformation potential, C_{2D} (Nm^{-1}) elastic modulus, m*/m effective mass and μ ($cm^2\ V^{-1}s^{-1}$) carrier mobility.

Direction	Carrier Type	E_1	C_{2D}	m^*/m_o	μ
Armchair	e	5.01	40.09	0.33	346
	h	5.28	40.09	0.43	292
Zigzag	e	4.72	86.25	0.23	1229
	h	7.86	86.25	0.13	890

Table-S4. Elastic properties of G- and P-InP_3 monolayer. (N/m)

	C_{11}	C_{22}	C_{12}	C_{66}	Y_{11}	Y_{22}
G-InP_3	48.35	48.37	18.11	15.13	41.57	41.57
P-InP_3	33.10	68.88	18.49	9.46	28.09	58.54

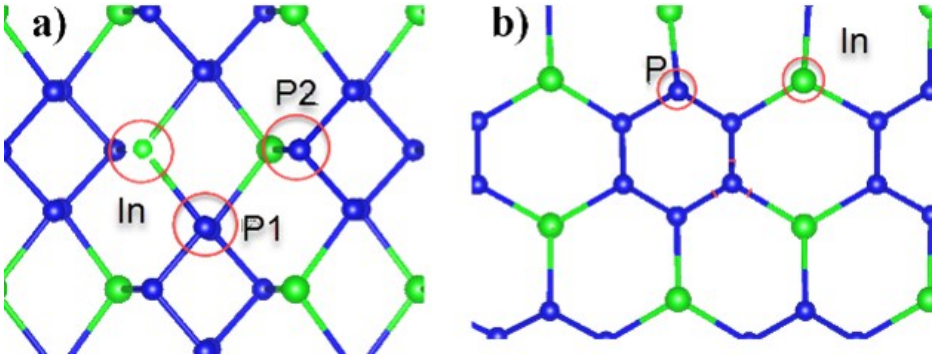

Figure S9. Different absorbed sites on (a) P-InP_3 and (b) G-InP_3 structure.

Table S5. Adsorption energies, Gibbs free energy ΔG_H, net charge gained of Hydrogen atom c and bond length of H-P bond.

Methods	**Adsorption sides**	**E_{ads}(eV)**	**ΔG(eV)**	**c_i (e)**	**Bond length (Å)**
DFT+D3	P1-atom	-0.17	0.12	0.34	1.427
PBE	P1-atom	-0.16	0.12	0.34	1.428

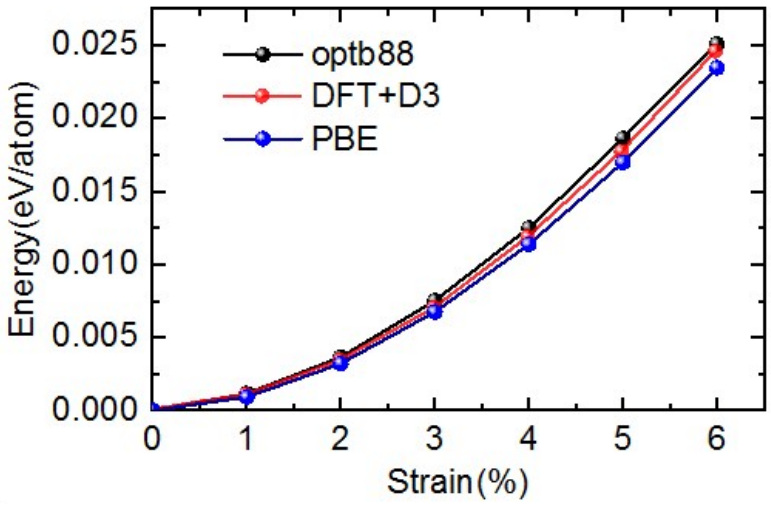

Figure S10. Energy change of P-InP_3 under biaxial strain ranging from 0% to +6%

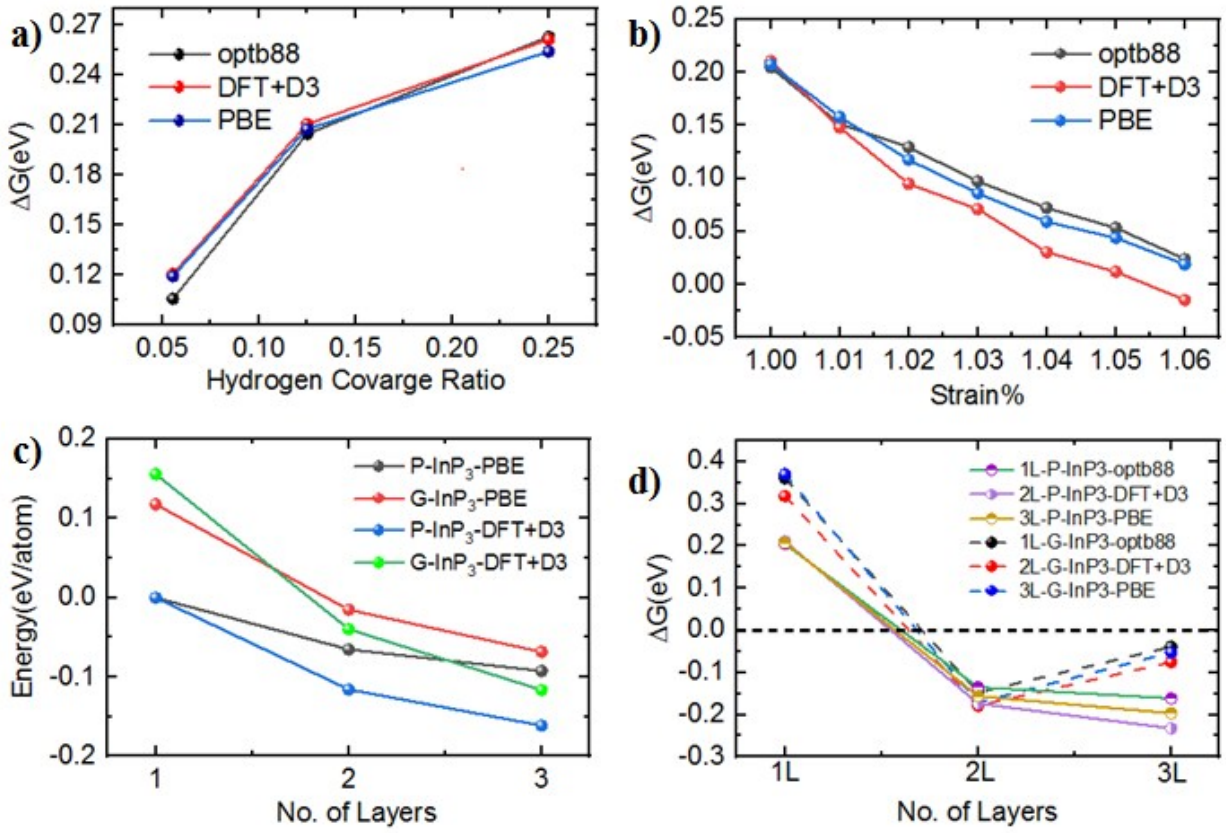

Figure S11. (a) The effect of hydrogen coverage ratio on Gibbs free energy of P-InP_3, (b) Effect of strain on Gibbs free energy, (c) Layers dependent energy of G & P-InP_3 structures, of which the energy of P-InP_3 is set to 0 eV/atom, (d) Effect of No. of layers on Gibbs free energy.

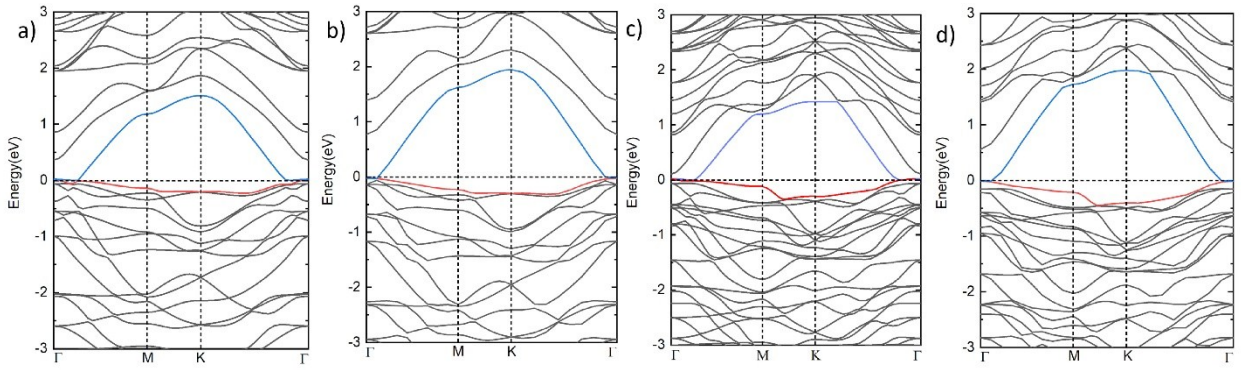

Figure S12. Bandstructure of G-InP_3 structures using functionals (a) 2L-InP_3 with optb88, (b) with HSE06+optb88, (c) 3L with optb88, (d) with HSE06+optb88

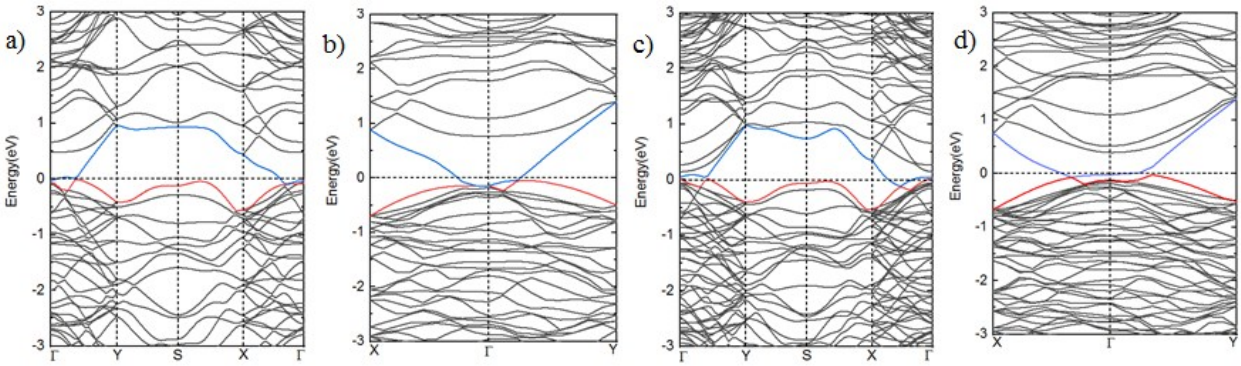

Figure S13. Bandstructure of P-InP_3 structures using functionals (a) 2L with optb88, (b) with HSE06+optb88, (c) 3L with optb88, (d) with HSE06+optb88

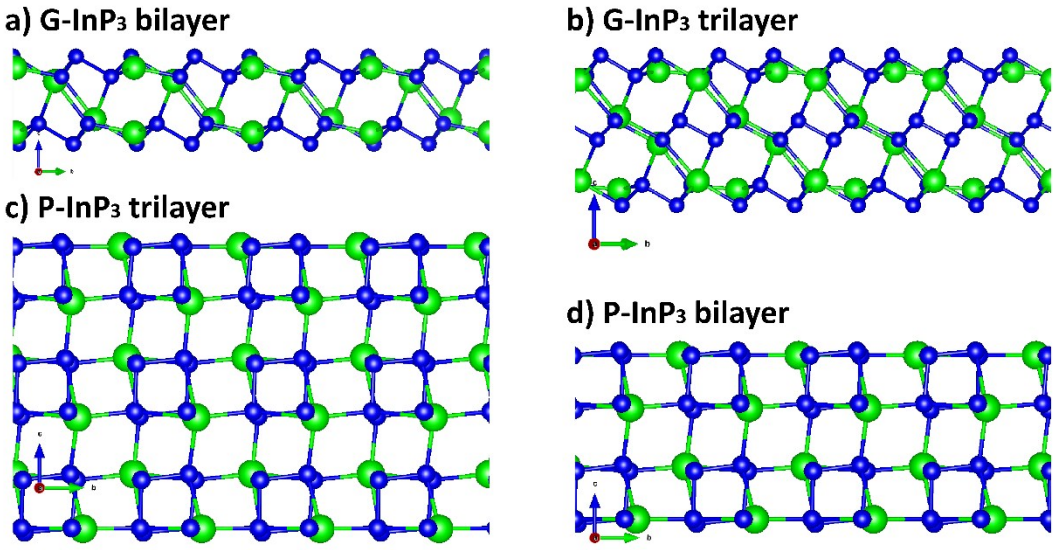

Figure S14. Side view of bilayer and trilayer of G-InP_3 and P-InP_3 structures

Table S6. Lattice parameters **a** & **b**, energy (vs. P-InP_3 monolayer (set as 0 eV/atom)) E.

Method	Structures	a(Å)	b(Å)	Energy(eV/atom)
optB88-vdW	P-2L-InP_3	7.60	8.21	-0.119
	P-3L-InP_3	7.58	8.19	-0.163
	G-2L-InP_3	7.53	7.53	-0.037
	G-3L-InP_3	7.54	7.54	-0.116
DFT+D3	P-2L-InP_3	7.56	8.09	-0.116
	P-3L-InP_3	7.55	8.07	-0.162
	G-2L-InP_3	7.49	7.49	-0.040
	G-3L-InP_3	7.51	7.51	-0.117
PBE	P-2L-InP_3	7.57	8.22	-0.065
	P-3L-InP_3	7.56	8.19	-0.092
	G-2L-InP_3	7.52	7.52	-0.016
	G-3L-InP_3	7.53	7.53	-0.069

Reaction energy barrier calculation

The partial geometric optimization method to scan the potential energy surface is to selectively and partially optimize the structure with fixing atoms positions on different free degrees by the selective dynamics setting in POSCAR of VASP.

As known, the Hydrogen evolution reaction is commonly considered in two elementary steps, the Volmer-Heyrovsky or Volmer-Tafel reactions, listed as below:

$$* + (H^+ + e^-) \rightarrow H* \qquad \text{Volmer step,}$$

$$H* + (H^+ + e^-) \rightarrow H_2 + * \qquad \text{Heyrovsky step,}$$

$$2H* \rightarrow H_2 + * \qquad \text{Tafel step,}$$

The reaction process in these four reactions is relatively simple, involved a few distance variations to be controlled. By changing the distance with small distance step of <0.2 Å for chemical bonding distance, and a smaller one for the range near barrier point, but a larger one for vdW interation range, we can obtain the potential energy surface of the reaction to profile a continuous reaction pathway to get a reaction energy barrier. For structure with water, we choose the same model successfully applied in previous work on MoS_2,[9] that the H^+ is attached on a water cluster of four H_2O. The atom distances of d_{H-P} and d_{H-O} for Volmer step on P-InP_3 and G-InP_3 are controlled by

fixing the position by limiting specific free degree of P…H…O three atoms during the geometric optimization, as shown in Figure S15. The controlled degree of four atoms (2H atoms and the connecting 2P atoms) for Tafel step on P-InP_3 is the distances of d_{P1-H1}, d_{In-H2} and d_{H1-H2}, as shown in Figure S16. And they are d_{P1-H1}~d_{P2-H2} and d_{H1-H2} for Tafel step on G-InP_3, d_{P-H1}, d_{O-H2} and d_{H1-H2} for Heyrovsky step on P-InP_3, and d_{P-H1}, d_{O-H2} and d_{H1-H2} for Heyrovsky step on G-InP_3, as shown in Figure S18, S17 and S19, respectively.

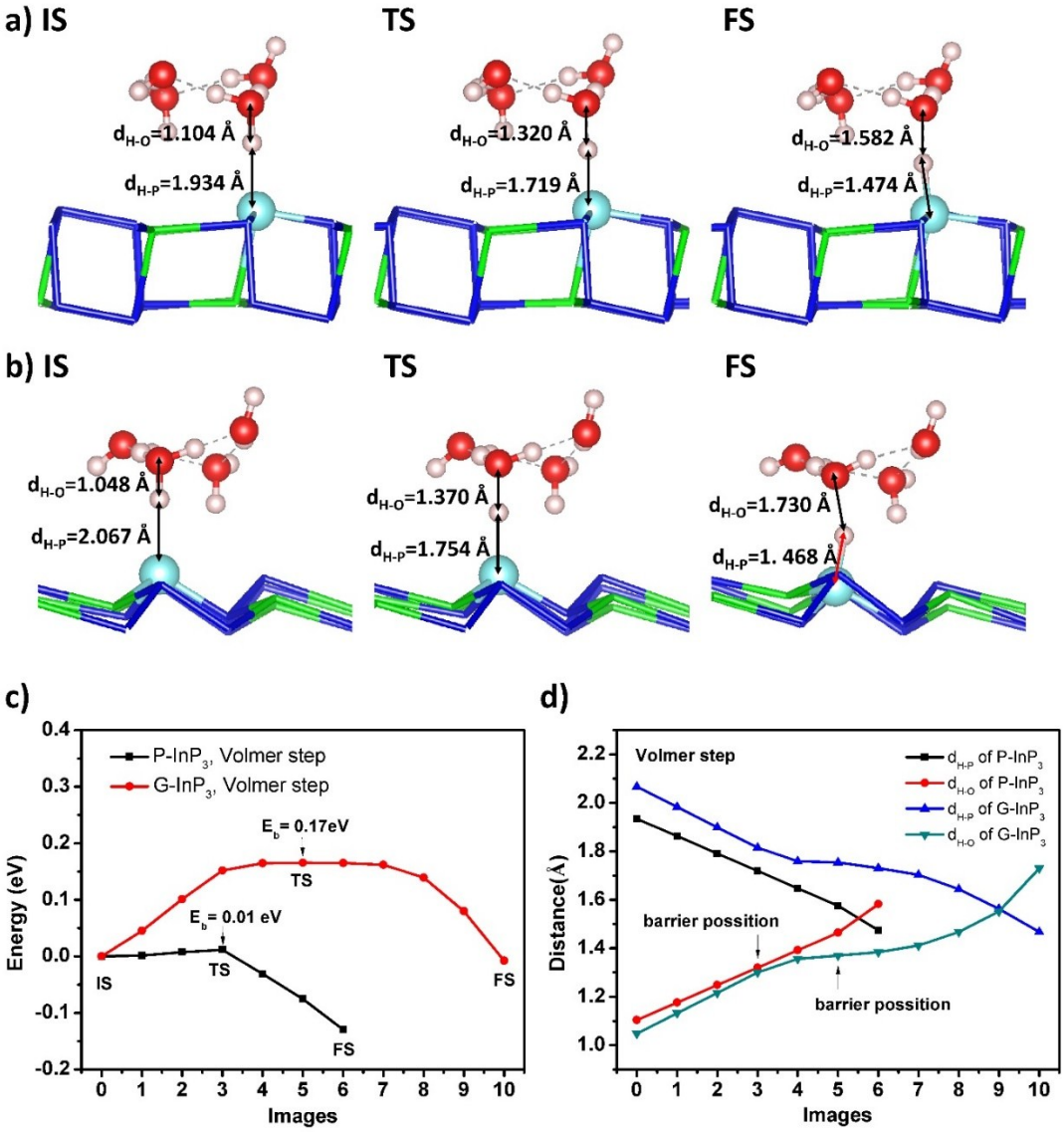

Figure S15. The Volmer step of HER on P-&G-InP_3. The structure details of initial state (IS), transition state (TS) and final state (FS) on (a) P-InP_3 and (b) G-InP_3. (c) The energy change (vs. initial state) from initial state (Image No.0) to final state (Image No.6 for P-InP_3 and No.10 for G-InP_3, respectively), of which the energy of initial state is set as 0 eV. (d) The distance change of d_{H-P} and d_{H-O} from initial state (Image No.0) to final state (Image No.6 for P-InP_3 and No.10 for G-InP_3, respectively).

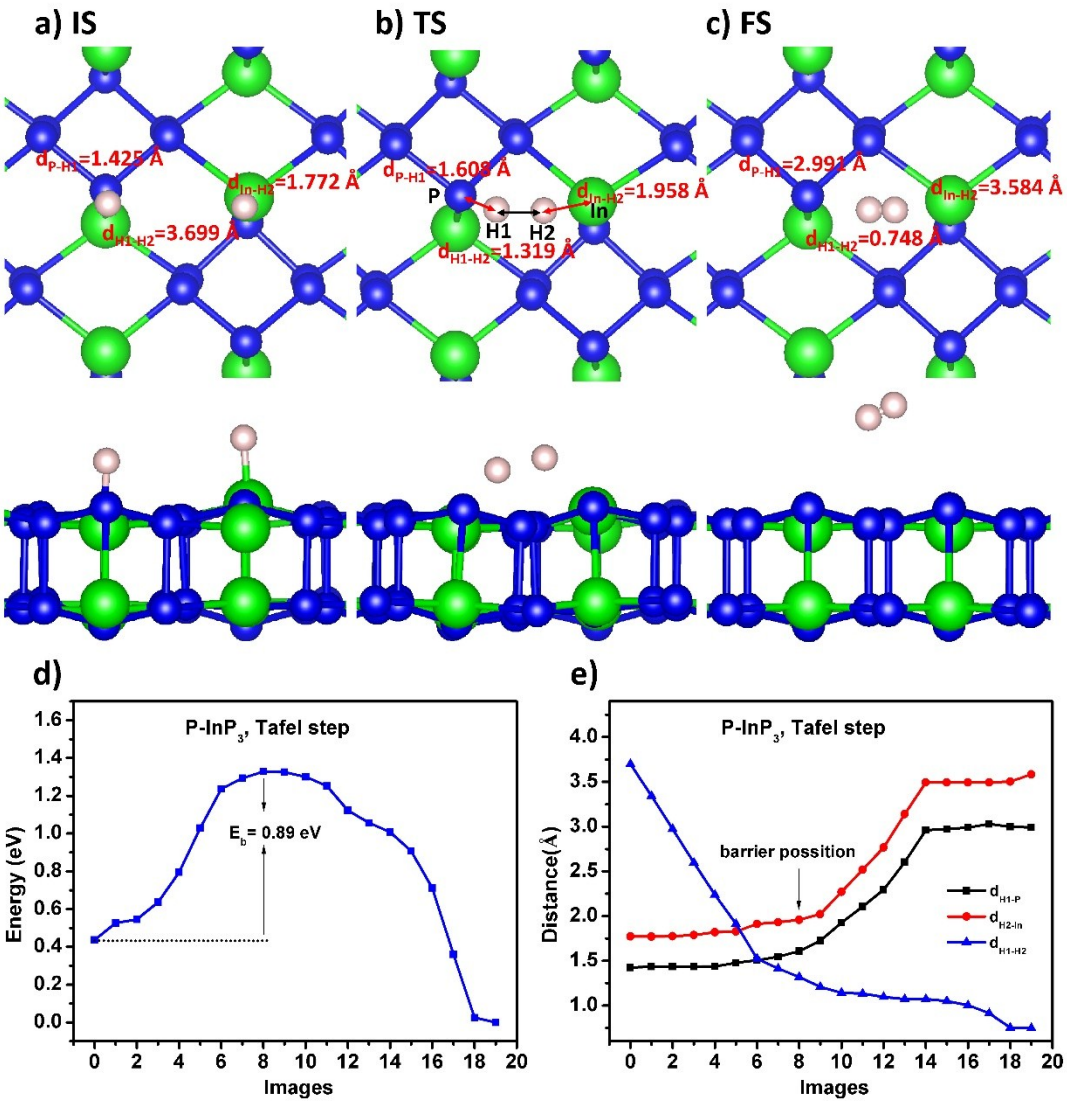

Figure S16. The Tafel step of HER on P-InP_3. The structure details of initial state (a), transition state (b) and final state (c). (d) The energy change (vs. final state) from initial state (Image No.0) to final state (Image No.19), of which the energy of final state is set as 0 eV. (e) The distance change of d_{P1-H1}, d_{In-H2} and d_{H1-H2} from initial state (Image No.0) to final state (Image No.19).

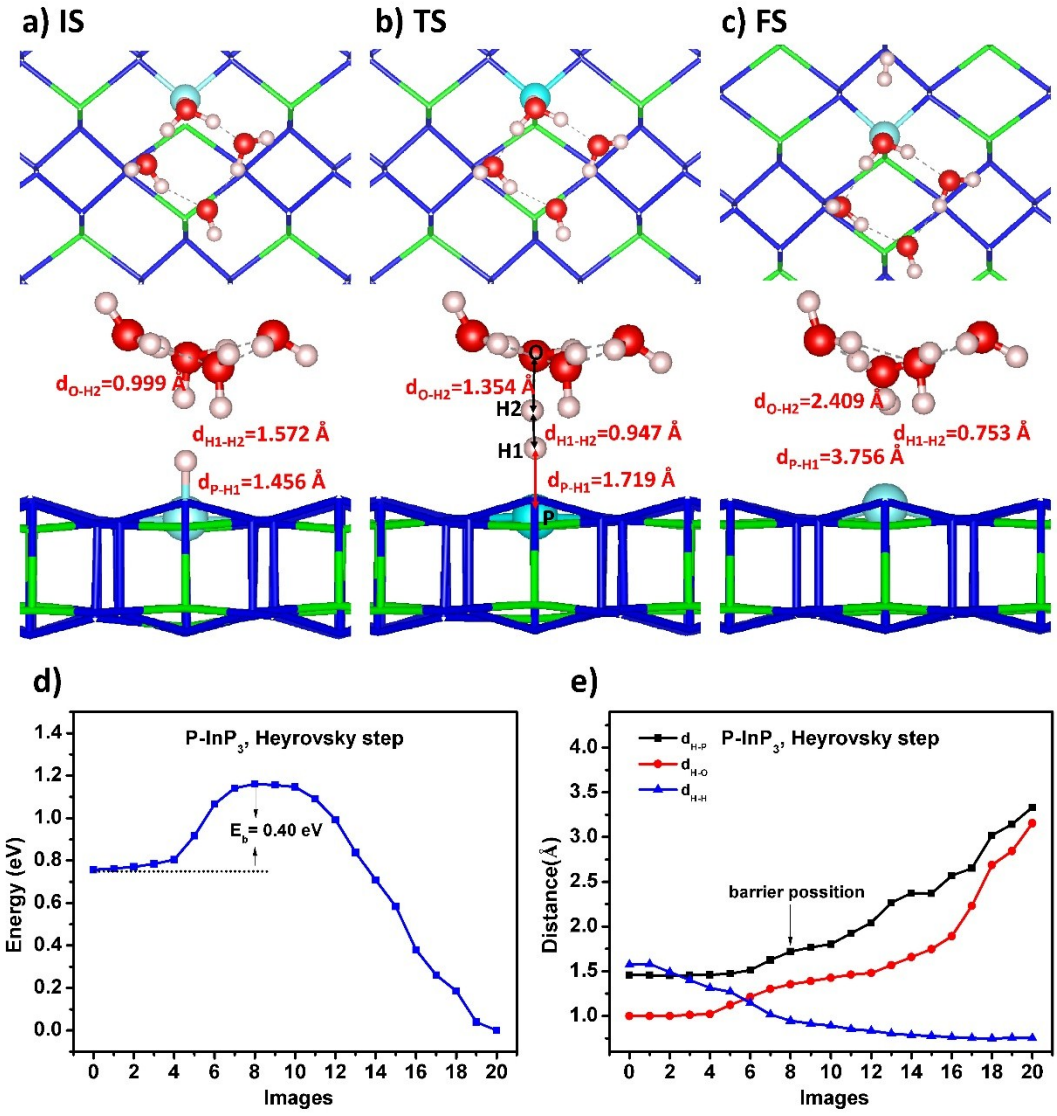

Figure S17. The Heyrovsky step of HER on P-InP_3. The structure details of initial state (a), transition state (b) and final state (c). (d) The energy change (vs. final state) from initial state (Image No.0) to final state (Image No.20), of which the energy of final state is set as 0 eV. (e) The distance change of d_{H1-P}, d_{H2-O} and d_{H1-H2} from initial state (Image No.0) to final state (Image No.20).

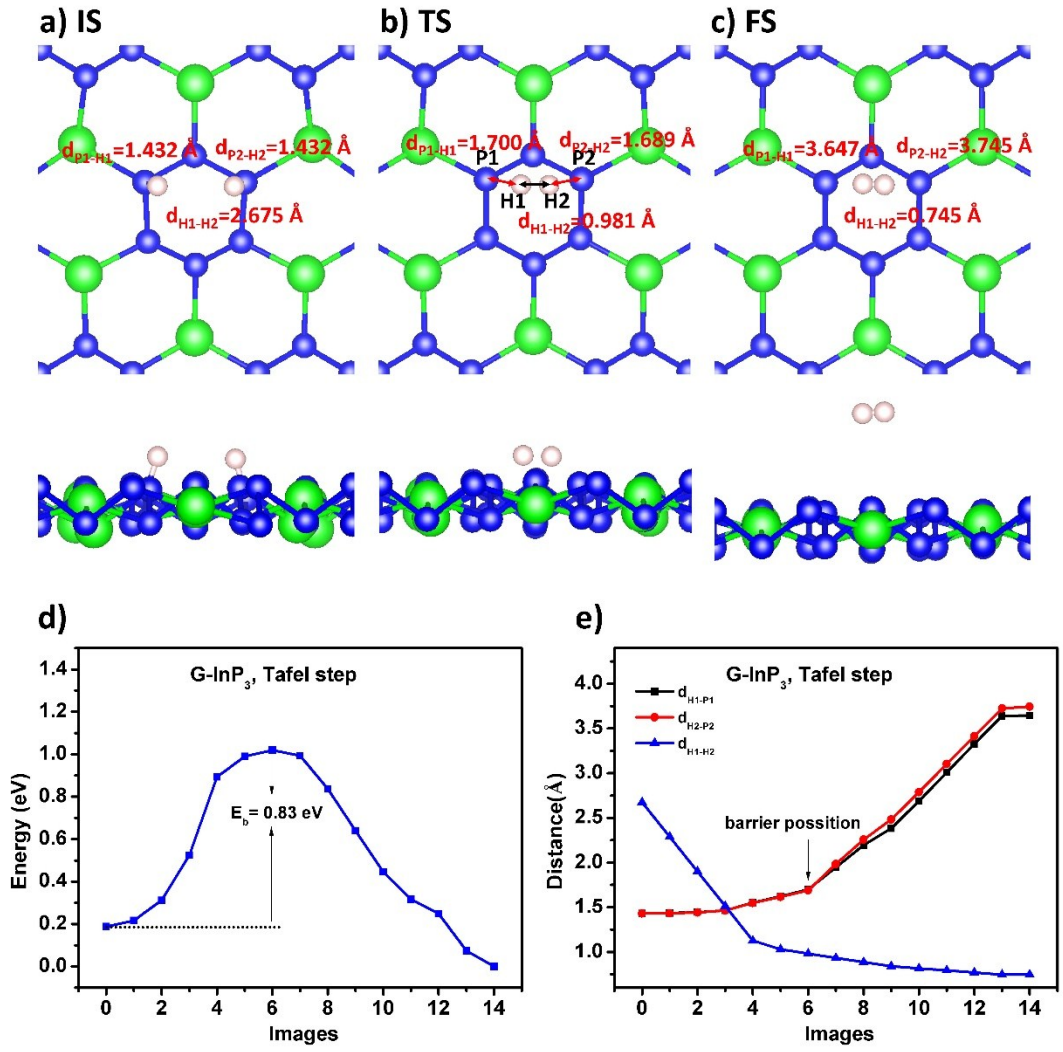

Figure S18. The Tafel step of HER on G-InP_3. The structure details of initial state (a), transition state (b) and final state (c). (d) The energy change (vs. final state) from initial state (Image No.0) to final state (Image No.14), of which the energy of final state is set as 0 eV. (e) The distance change of d_{P1-H1}, d_{P2-H2} and d_{H1-H2} from initial state (Image No.0) to final state (Image No.14).

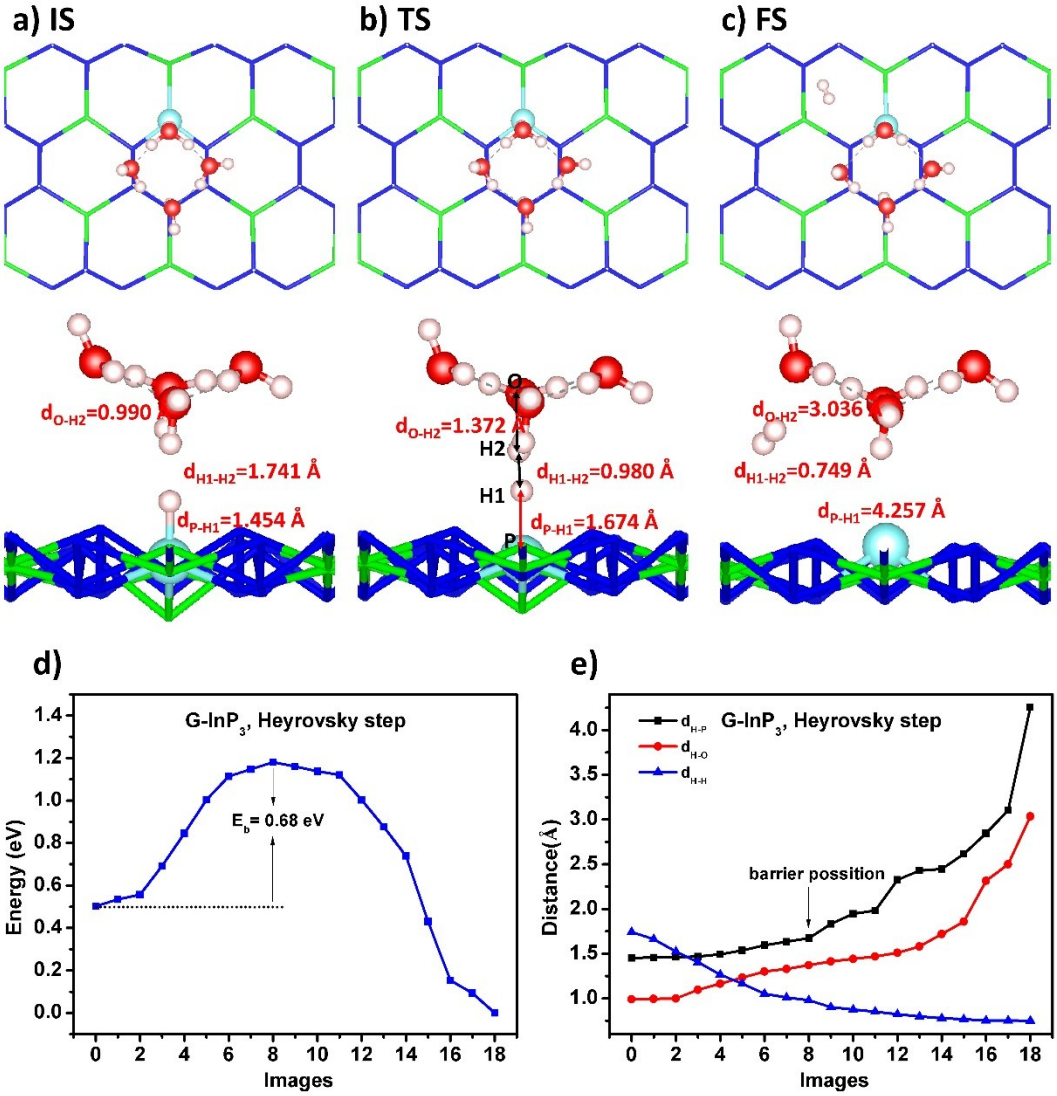

Figure S19. The Heyrovsky step of HER on G-InP$_3$. The structure details of initial state (a), transition state (b) and final state (c). (d) The energy change (vs. final state) from initial state (Image No.0) to final state (Image No.18), of which the energy of final state is set as 0 eV. (e) The distance change of d_{H1-P}, d_{H2-O} and d_{H1-H2} from initial state (Image No.0) to final state (Image No.18).

References:

1. J. H. Jung, C.H. Park and J. Ihm, *Nano Lett.*, 2018, **18**, 2759-2765.

2. J. Bardeen and W. Shockley, *Phys. Rev.*, 1950, **80**, 72-80.

3. M. Long, L. Tang, D. Wang, L. Wang and Z. Shuai, *J. Am. Chem. Soc.*, 2009, **131**, 17728–17729.

4. S. Bruzzone and G. Fiori, *Appl. Phys. Lett.*, 2011, **99**, 222108.

5. X. L. Yang, X. J. Ye, C. S. Liu and X. H. Yan, *J. Phys. Condens. Matter*, 2018, **30**, 065701.

6. M. Qiao, Y. Chen, Y. Wang and Y. Li, *J. Mater. Chem. A*, 2018, **6**, 4119-4125.

7. Z. W. Teng, C. S. Liu and X. H. Yan, *Nanoscale*, 2017, **9**, 5445-5450.

8. N. Lu, Z. Zhuo, H. Guo, P. Wu, W. Fa, X. Wu and X. C. Zeng, *J. Phys. Chem. Lett.*, 2018, **9**, 1728-1733.

9. Y. Huang, R. J. Nielsen, W. A. Goddard and M. P. Soriaga, *J. Am. Chem. Soc.*, 2015, **137**, 6692-6698.